International Conference on Tropical Studies and Its Applications (ICTROPS)
Volume 5, (2026), e-ISSN : xxxx-xxxx
Website: http://e-journals2.unmul.ac.id/index.php/ictrops
Resilient Tropical Futures: Digital Transformation, Green Infrastructure, and Climate Adaptation

Modeling and Simulation of Nanofiltration for Separating Calcium, Magnesium, and Sulfate from Rejected Brine to Produce High-Purity Salt

Mohamad Sugianto[1]*, Ali Altway[2], and Susianto[3]

[1,2,3]Department of Chemical Engineering, Faculty of Industrial Technology and Systems Engineering, Institut Teknologi Sepuluh Nopember, Surabaya, East Jawa, 60111, Indonesia

**Corresponding author Email: 6008232002@student.its.ac.id*

The manuscript was received on November 17th, 2025, revised on December 3rd, 2025, and accepted on January 05th, 2026, date of publication February 02nd, 2026

Abstract

Rejected brine from seawater desalination is a concentrated stream rich in NaCl but containing elevated levels of Ca^{2+}, Mg^{2+}, and SO_4^{2-} that limit its use as a feed for high-purity industrial salt. This study aims to evaluate whether nanofiltration can selectively remove these divalent ions and to provide a mechanistic description of ion transport and process performance. A steady-state, isothermal model of a commercial spiral-wound KeenSen NF1-4040F element is developed using the Donnan-Steric Pore Model with Dielectric Exclusion coupled to the Extended Nernst–Planck equations. Radial transport inside the pores is coupled with axial mass balances for the feed and permeate streams, and solved numerically over feed pressures of 2.5 - 12.5 bar and inlet flow rates of 1.08 - 3.60 $m^3 \cdot h^{-1}$. The simulations predict that permeate-water flux increases linearly with pressure, while along the module the retentate flow rate decreases and the permeate flow rate increases linearly with axial position. Stage recovery rises with pressure but decreases with increasing inlet flow rate. Mechanistic flux decomposition indicates that convection dominates cation transport, particularly for Na^+, whereas diffusion and electromigration contribute more strongly to the transport of anions. Under the investigated conditions, sulfate and magnesium achieve rejections above 97%, calcium about 96%, while chloride and sodium show lower but still significant rejections. Overall, the model suggests that operating at moderate-to-high pressure and moderate inlet flow can maximise recovery while maintaining high divalent-ion rejection, supporting the use of nanofiltration as a pre-purification step to upgrade rejected brine to a higher-purity salt feedstock.

Keywords: *DSPM-DE; Industrial salt; Ion transport modeling; Nanofiltration; Rejected brine.*

1. Introduction

Industrial salt is a fundamental inorganic commodity that functions as a reactant, electrolyte, or processing aid in many process industries, including chlor-alkali production, food and beverage manufacture, textiles, leather processing, water treatment, and pharmaceuticals. In Indonesia, national demand for industrial-grade salt has been estimated at approximately 3.8 - 4.0 million ton per year, yet domestic production of high-purity salt remains insufficient, so that a large fraction of demand is still met through imports. The chlor-alkali, glass, and related chemical sectors consume the majority of this salt and require feedstocks with high NaCl content and very low concentrations of divalent cations such as Ca^{2+} and Mg^{2+} in order to prevent scaling, membrane fouling, and defects in product quality [1]. Consequently, the identification and development of alternative, higher-purity salt feed sources is strategically important for reducing import dependence and enhancing the resilience of Indonesia's process-industry supply chains.

One underexploited candidate for such a feed is the concentrated brine rejected from seawater desalination plants. Global seawater desalination capacity has increased rapidly, particularly in arid and coastal regions, and this expansion has been accompanied by large volumes of high-salinity brine that are typically discharged back into the marine environment. Recent assessments indicate that desalination facilities generate more than 140 million m^3 of brine per day, often with salinity up to about twice that of ambient seawater and containing residual process chemicals and trace metals [2][3]. If released without adequate management, this effluent can raise local salinity and temperature, alter marine community structures, and degrade coastal ecosystems. At the same time, the high ionic strength and significant NaCl content of rejected brine make it an attractive target for valorisation through resource recovery and industrial salt production, consistent with zero-liquid-discharge and circular-economy concepts [3].

The main technical barrier to upgrading rejected brine into industrial-grade salt is the selective removal of divalent cations such as Ca^{2+} and Mg^{2+}, which promote hygroscopic behaviour, caking, and scaling, thereby limiting the usability of the final product in chlor-alkali and other sensitive applications. Membrane nanofiltration (NF) is particularly well suited to this separation because its performance lies

between reverse osmosis (RO) and ultrafiltration (UF): NF commonly operates at lower transmembrane pressures than RO, offers higher water fluxes, and exhibits pronounced preferential rejection of multivalent ions over monovalent ions [4][5]. Studies on NF treatment of RO brine and diluted seawater have reported 79 - 89% removal of total dissolved solids (TDS) and 96 - 98% removal of total hardness, with especially high retention of Ca^{2+} and Mg^{2+}, demonstrating that NF can serve as an effective pre-treatment or stand-alone step for brine valorisation and scale control [5][6]. Further work has applied NF directly to desalination brines to recover water and suppress scaling precursors, often achieving high divalent-ion rejection at moderate pressure and recovery conditions [7].

Designing NF systems that can consistently upgrade rejected brine into a suitable salt feedstock requires more than empirical performance curves; it calls for a mechanistic description of transport and exclusion phenomena in charged nanopores. Over roughly the past two decades, the Donnan Steric Pore Model with Dielectric Exclusion (DSPM-DE) has emerged as a comprehensive framework for representing ion and water transport in NF membranes. In this approach, the Extended Nernst-Planck (ENP) equations are solved for each ionic species, accounting for diffusion, convection, and electromigration within the pores, while ion partitioning at the membrane–solution interface is described through Donnan electrostatic exclusion, steric hindrance, and a dielectric exclusion term derived from differences in Born solvation energy between the pore phase and the bulk solution [8][9][10]. Classical contributions by Bowen and co-workers established the DSPM-DE architecture and emphasised the importance of dielectric exclusion for multivalent-ion selectivity, and more recent studies have extended the framework to investigate temperature effects, membrane charge and pore-size distributions, and the relative impacts of Donnan versus dielectric exclusion [8][10].

DSPM-DE has recently been applied to increasingly complex NF systems, including multicomponent feed and membranes with tailored composition. [11] Cevallos-Cueva and co-authors (2025), for example, used DSPM-DE to analyse nitrate-selective NF membranes and showed that dielectric exclusion and diffusion jointly govern sulfate rejection, leading to very high SO_4^{2-} retention (≈96 - 99%) while allowing partial passage of NO_3^-; under certain conditions, coupled transport phenomena even yielded negative apparent rejection of nitrate. In a subsequent study, the same group examined Na^+ / Mg^{2+} selectivity in interfacially polymerised NF membranes and demonstrated how adjusting piperazine and trimesoyl chloride concentrations modifies membrane charge density and pore structure, and in turn the Na^+ / Mg^{2+} separation factor, again using DSPM-DE as the modelling core. These examples illustrate how mechanistic modelling can link membrane formulation, operating variables, and multicomponent ion transport in a physically interpretable way.

Despite these advances, most published DSPM-DE studies still focus on idealised conditions, such as synthetic salt solutions, potable-water treatment, or the removal of specific contaminants, and only a limited number address realistic rejected-brine compositions that contain Na^+, Cl^-, Ca^{2+}, Mg^{2+}, and SO_4^{2-} at salinity levels typical of seawater desalination plants [3][5]. Moreover, relatively few works explicitly couple the radial (pore-scale) transport description of DSPM-DE with axial mass-balance equations along spiral-wound modules to explore process-level metrics such as recovery, axial concentration profiles, and trade-offs between divalent-ion rejection and operating conditions. There is therefore a need for mechanistic models that can (i) capture the selective removal of Ca^{2+} and Mg^{2+} from realistic rejected brine, (ii) resolve the relative contributions of diffusion, convection, and electromigration to overall ion transport, and (iii) generate operating maps that are directly useful for designing NF-based routes to high-purity industrial salt.

In response to this gap, the present study develops a steady-state, isothermal mechanistic model for a commercial spiral-wound nanofiltration element (KeenSen NF1-4040F) treating rejected brine containing Na^+, Cl^-, Ca^{2+}, Mg^{2+}, and SO_4^{2-}. The model is based on the DSPM-DE framework, solving the Extended Nernst–Planck equations in the pore (radial) direction coupled with axial mass balances for the feed and permeate streams, and is implemented numerically in MATLAB over a range of feed pressures and inlet flow rates. The objectives are to predict fluxes, concentration profiles, and ion rejections along the module, to decompose the transport mechanisms of each ion, and to construct an operating window that maximises water recovery while maintaining high rejection of divalent ions. In doing so, the study aims to support the valorisation of rejected brine as a cleaner, more sustainable feedstock for industrial salt production and to provide a realistic, process-oriented case study of DSPM-DE modelling for nanofiltration.

2. Materials and Methods

2.1. Modeled System and Operating Conditions

This The nanofiltration (NF) module is represented as an equivalent flat “unwound” leaf of a spiral-wound KeenSen NF1-4040F element. Cross-flow occurs along the axial coordinate $z \in [0, L]$ in the feed channel, while solvent and ion transport through the active layer are resolved in the radial coordinate $x \in [0, \delta_x]$. The electrolyte contains five ionic species, Na^+, Cl^-, Ca^{2+}, Mg^{2+}, and SO_4^{2-}, which are assumed to satisfy local electroneutrality everywhere inside the pore solution. Steady-state, isothermal conditions ($T = 298.15$ K) are imposed, with the brine treated as an incompressible Newtonian fluid of constant bulk density and viscosity over the operating range, consistent with mechanistic NF models for spiral-wound leaves in the literature [12][13].

The feed composition is based on a representative rejected brine stream. On a molar concentration basis (mol·m^{-3}), the inlet feed contains Na^+ = 466.01, Cl^- = 681.04, Ca^{2+} = 7.78, Mg^{2+} = 38.99, and SO_4^{2-} = 31.80. The bulk solution density and viscosity are taken as $\rho = 1030.6$ kg·m^{-3} and $\mu = 1.96$ mPa·s, respectively, while Stokes radii and bulk diffusivities for each ion follow Labban et al. (2017) and related low-pressure NF characterization work [14][15].

Operating conditions span a practical window for brine valorization. The feed pressure P_f is varied between 2.5, 5.0, 7.5, 10.0, and 12.5 bar (absolute), while the inlet feed flow rate $Q_{f,}$ ranges from 1.08 to 3.60 m^3·h^{-1}. The permeate pressure P_p is maintained at 1.01325 bar. These conditions cover moderate-pressure NF typical of brine polishing and divalent–monovalent fractionation, comparable to recent RO-brine NF studies where divalent hardness and sulfate are selectively removed [6][16].

2.2. Physical Parameters and Osmotic Pressure

Membrane and module parameters are chosen to represent a commercial spiral-wound NF element in desalination pre-/post-treatment. The active layer is modeled as a charged, cylindrical-pore medium with effective pore radius $r_{pore} \approx 0.43$ nm and the active-layer thickness $\delta_x = 1\,\mu$ m, while the fixed volumetric charge density is set to $C_x \approx -45$ mol·m^{-3}, typical for negatively charged thin-film composite NF membranes operating with multi-ionic brines [17][18]. The effective membrane area per element is $A_{mem} = 7.2$ m^2, the module length is $L = 1.016$ m, and the feed-channel hydraulic height is $d_h = 100\,\mu$m, which yields an equivalent channel cross-section $A_{ch} \approx A_{mem}L^{-1} = 7.09 \times 10^{-4}$ m^2.

Permeate-water flux J_w is computed from a Poiseuille-type relation for flow through the active layer,

$$J_w = K_{\mathrm{perm}}\left[\left(P_f - P_p\right) - f\,\Delta\pi\right] \tag{1}$$

where the hydraulic permeability is

$$K_{\mathrm{perm}} = \frac{r_{\mathrm{pore}}^2}{8\mu\delta_x} \approx 1.18 \times 10^{-11}\,\mathrm{m\ Pa^{-1}s^{-1}} \tag{2}$$

and $f \in [0,1]$ is an effective osmotic factor used to interpolate between a purely hydraulic response ($f = 0$) and the full osmotic pressure difference $\Delta\pi$. Similar forms for J_w are standard in DSPM-DE-based NF models for charged membranes [10][19].

The osmotic pressure difference is evaluated from the wall concentrations on the feed and permeate sides obtained from the concentration-polarization (CP) model. For each side s (feed or permeate), the solution osmotic pressure is approximated using a van 't Hoff expression,

$$\pi_w^{(s)} = RT\sum_i \nu_i C_{i,w}^{(s)} \tag{3}$$

and the driving osmotic difference is

$$\Delta\pi = \pi_w^{(\mathrm{feed})} - \pi_w^{(\mathrm{perm})} \tag{4}$$

Here R is the universal gas constant, $T$is the absolute temperature, ν_i is the van 't Hoff factor for ion i, and $C_{i,w}^{(s)}$ is the wall concentration at side s. This formulation is widely used in mechanistic NF analyses of multi-ionic brines and SWRO retentates [14][20].

2.3. Physical Parameters and Osmotic Pressure

Ion transport inside the charged pores is described by the Donnan Steric Pore Model with Dielectric Exclusion (DSPM-DE), written in the framework of the Extended Nernst-Planck (ENP) equation. The total molar flux of ion i, J_i, is the sum of convection, diffusion, and electromigration,

$$J_i = K_{ic}\,C_i\,J_w - D_i^e\,\frac{dC_i}{dx} - \frac{z_iF}{RT}\,D_i^e\,C_i\,\frac{d\psi}{dx} \tag{5}$$

where K_{ic} is a convective hindrance factor, $D_i^e = K_{id}D_{i,\infty}$ is the effective diffusivity in the pore (with K_{id}a diffusive hindrance factor and $D_{i,\infty}$, the bulk diffusivity), $z_i$is ion valence, F_{is} Faraday's constant, and $\psi(x)$ is the dimensionless electrostatic potential. This formulation follows earlier DSPM-DE developments for NF membranes treating multi-ion solutions [19][21][22].

Concentration polarization at the feed-side wall is accounted for through a film model. For each ion, the wall concentration on the feed side is

$$C_{i,w} = \mathrm{C_{i,bulk}}\exp\left(\frac{J_w}{k_m}\right) \tag{6}$$

where the mass-transfer coefficient k_m obtained from a Sherwood correlation,

$$k_m = \frac{\mathrm{Sh}\,D_{i,\infty}}{d_h},\ \mathrm{Sh} = 0.079\,\mathrm{Re}^{0.8}\mathrm{Sc}^{0.33} \tag{7}$$

with Reynolds and Schmidt numbers defined in the usual way from local channel hydrodynamics. Such CP correlations are commonly used in NF modeling for desalination and brine management [15].

Ion partitioning at the membrane interfaces is described by Donnan equilibrium combined with steric and dielectric exclusion. On each side $\mathrm{s} \in \{\mathrm{feed}, \mathrm{perm}\}$, the concentration at the membrane side of the interface is

$$\mathrm{C_{i,mem}^s} = \Phi_\mathrm{i}\Phi_{\mathrm{B,i}}\mathrm{C_{i,w}^{(s)}}\exp\left(-\frac{\mathrm{z_iF}}{\mathrm{RT}}\Psi_\mathrm{D}^{(\mathrm{s})}\right) \tag{8}$$

where $\Phi_i = (1-\lambda_i)^2$ is the steric partition coefficient with $\lambda_i = r_i/r_{pore}$, $\Phi_{B,i}$ is a Born factor accounting for the dielectric contrast between bulk solution and pore fluid, and $\psi_D^{(s)}$ is the Donnan potential at side s. The Donnan potentials are obtained from electroneutrality at each membrane interface,

$$\sum_i z_i C_{i,mem}^{(S)} + C_x = 0 \quad (9)$$

Inclusion of $\Phi_{B,i}$ implements dielectric exclusion in the sense of DSPM-DE and has been shown to be essential to capture multivalent-ion rejection in NF and negative rejections in certain co-ion systems [10][17][21]

Equations (5), together with electroneutrality in the pore and the expression for J_w, define a coupled system of ordinary differential equations (ODEs) for $\psi(x)$ and $C_i(x)$ across the active layer. Boundary conditions are set by the interface concentrations and Donnan potentials: $\Psi(0) = \Psi_D^{(feed)}$, $C_i(0) = C_{i,mem}^{(feed)}$, $\Psi(\delta_x) = \Psi_D^{(perm)}$, and $C_i(\delta_x) = C_{i,mem}^{(perm)}$. The Donnan potentials $\psi_D^{(s)}$ are obtained by solving Eq. (9) via root-finding at each interface. This approach follows recent mechanistic DSPM-DE analyses for nitrate-selective and brine-treatment NF membranes [17][23].

2.4. Axial Module Model and Performance Indicators

Figure 1 illustrates the equivalent "unwound" flat-sheet representation of the spiral-wound nanofiltration element used in this work. The membrane leaf has length L and width W, with a thin active layer of thickness Δx separating the feed channel (height, h_f) from the permeate channel (height, h_p). Feed solution enters at $z = 0$ with volumetric flow rate $Q_{f,in}$ and bulk concentrations $C_{i,in}$, while permeate is collected along the permeate channel and exits at $z = L$ with flow rate $Q_p(L)$. The schematic also highlights the local solvent flux $J_w(z)$ and solute fluxes $J_i(z)$ across the membrane, which couple the radial transport model to the axial mass balances. This geometric idealization follows the flat-sheet / spiral-wound formulation used in large-scale DSPM-DE simulations of seawater nanofiltration [12].

For numerical solution, the module is discretized into Naxial control volumes of equal length $\Delta z = L/N$. Each segment k (with axial coordinate z_k) is associated with a membrane area

$$A_{seg} = \frac{A_{mem}}{L}\Delta z \quad (10)$$

where A_{mem} is the total active membrane area of the element. Within each segment, the radial DSPM-DE model provides the local solvent flux $J_w(k)$ and ion fluxes $J_i(k)$, which are assumed uniform over A_{seg} for that segment. This finite-volume coupling between local pore transport and axial bulk flow is standard in mechanistic NF simulations and has been successfully applied to multi-ionic feeds such as seawater and ion-exchange regenerant solutions [12][20].

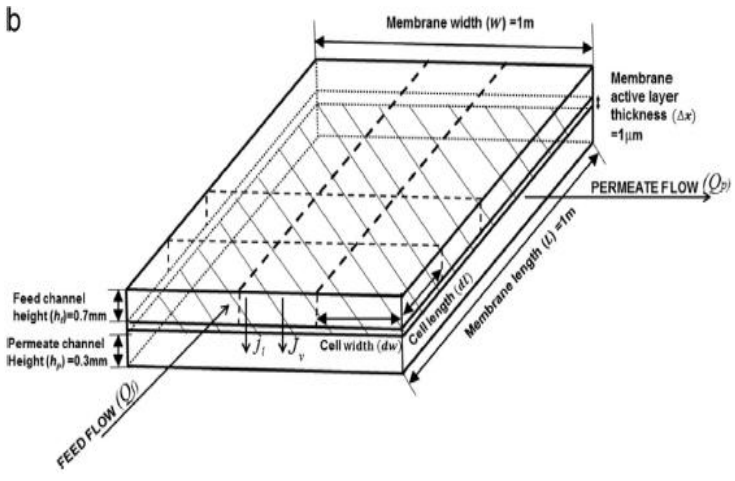

Fig 1. Schematic of the equivalent flat-sheet representation of the spiral-wound NF leaf, showing membrane length L, width W, active-layer thickness Δx, feed and permeate channel heights (h_f and h_p), and the axial variation of feed and permeate flow rates $Q_f(z)$ and $Q_p(z)$ [12].

The axial water-flow balances for feed and permeate streams across segment $k \rightarrow k+1$are written as

$$Q_f(k+1) = Q_f(k) - J_w(k)\,A_{seg} \quad (11a)$$
$$Q_p(k+1) = Q_p(k) + J_w(k)\,A_{seg} \quad (11b)$$

where $Q_f(k)$ and $Q_p(k)$ are the segment-inlet flow rates of the feed and permeate, respectively. These relations enforce conservation of water: the volume that permeates through the membrane in each segment is subtracted from the feed channel and added to the permeate

channel. Similar axial balance formulations are widely used in spiral-wound NF and RO modeling to capture the gradual increase of recovery and concentration along the feed path.

For each ionic species i, the discrete component mass balances in the retentate and permeate channels over segment k are formulated to match the thesis model exactly. The retentate balance is

$$C_{i,R}^{(k+1)} = C_{i,R}^{(k)} + \frac{-J_i^{(k)} A_{seg} - C_{i,R}^{(k)}\left(Q_f^{(k+1)} - Q_f^{(k)}\right)}{\max\left(10^{-30}, Q_f^{(k)}\right)} \tag{12}$$

and the permeate balance is

$$C_{i,P}^{(k+1)} = C_{i,P}^{(k)} + \frac{J_i^{(k)} A_{seg} - C_{i,P}^{(k)}\left(Q_p^{(k+1)} - Q_p^{(k)}\right)}{\max\left(10^{-30}, Q_p^{(k)}\right)} \tag{13}$$

Here $C_{i,R}(k)$ and $C_{i,P}(k)$ are the bulk concentrations of species $i$in the retentate and permeate channels at the inlet of segment k, and the small denominator cut −off avoids numerical division by zero at the module inlet. The first term in each numerator accounts for the net radial flux $J_i(k)\,\mathrm{A_{seg}}$, while the second term represents dilution or concentration effects caused by the axial change in volumetric flow. This discrete formulation is equivalent to integrating the differential component balances along $z$under the assumptions of plug flow and negligible axial dispersion, which are typical for cross-flow nanofiltration modules [19].

At the module outlet $z = L$, two key performance indicators are evaluated. The stage recovery is defined as

$$\mathrm{Rec} = \frac{Q_p(L)}{Q_{f,in}} \tag{14}$$

which measures the fraction of the incoming feed converted to permeate. The overall rejection of ion $i$is calculated from the ratio of outlet molar flow rates in the permeate and retentate streams,

$$\%R_i = 100\left[1 - \frac{\dot{n}_{i,P}(L)}{\dot{n}_{i,R}(L)}\right] \tag{15}$$

$$\dot{n}_{i,P}(L) = Q_p(L)\, C_{i,P}(L) \tag{16a}$$

$$\dot{n}_{i,R}(L) = Q_f(L)\, C_{i,R}(L) \tag{16b}$$

These definitions are consistent with common practice in NF modeling and experimental characterization, facilitating comparison with literature data on multi-ionic separations and on the performance of commercial nanofiltration membranes [20], [23].

2.5. Numerical Solution Strategy and Model Verification

The DSPM-DE + ENP system in the radial coordinate is solved using MATLAB's explicit ODE45 solver, an adaptive Runge-Kutta (4, 5) method, with relative and absolute tolerances set to $10^{-7}$and 10^{-9}, respectively. For each axial segment, the CP correlation is evaluated from the local cross-flow conditions, the Donnan potentials at both interfaces are obtained from Eq. (9) via a scalar root-finding routine, and the resulting initial conditions are used to integrate the ODE system for $\psi(x)$ and $C_i(x)$ across the active layer. The resulting $J_w^{(k)}$ and $J_i^{(k)}$are then passed to the axial marching scheme (Eqs. (11) - (13)) to advance from segment k to $k+1$ until $z = L$. This iterative CP-Donnan-ODE coupling per segment is consistent with recent DSPM-DE implementations for spiral-wound NF modules [12][23].

At the module inlet, initial conditions are set to $Q_f(0) = C_{f,in}$, $Q_p(0) = 0$, $C_{i,R}(0) = C_{i,feed}$, and $C_{i,P}(0) = 0$. In selected scenarios, an effective osmotic factor f is calibrated by bisection within a bounded interval $[0, f_{\max}]$ to match a target overall recovery (e.g., 15%) with a tolerance of 5×10^{-4}. For pure hydraulic tests, f is set to zero in Eq. (1) to highlight the linear response of J_w to P_f. Similar strategies have been used to tune effective osmotic contributions in NF simulations of brine-valorization trains [12][14].

Internal verification includes (i) approximately linear J_w - P_f behavior in the purely hydraulic limit, (ii) overall mass balance closure with total mass-flow discrepancies well below 0.1%, (iii) absence of negative values for concentrations or flow rates, and (iv) physically consistent axial trends (monotonic decrease of $Q_f(z)$, increase of $Q_p(z)$, and progressive concentration of $C_{i,R}(z)$. External validation is performed by comparing predicted recoveries and ion rejections against data and trends from NF studies on RO brines and multi-ionic feeds of comparable salinity and composition [6][17][20][23].

3. Results & Discussion

3.1. Hydrodynamic Behavior: Water-Flux Response to Feed Pressure and Module Mass Balance

We first verify that the simulated hydraulics of the KeenSen NF1-4040F element behave in a physically consistent way. Figure 2 shows the permeate-water flux J_w as a function of feed pressure P_f in the range 2.5 - 12.5 bar for a representative inlet flow rate. The model predicts an almost linear increase of J_w with P_f, which reflects a nearly constant hydraulic permeability L_p and limited membrane compaction within this pressure window. This behaviour is in line with experimental nanofiltration studies, where pure-water flux is typically proportional to the effective transmembrane pressure until either compaction or strong concentration-polarization effects appear [24].

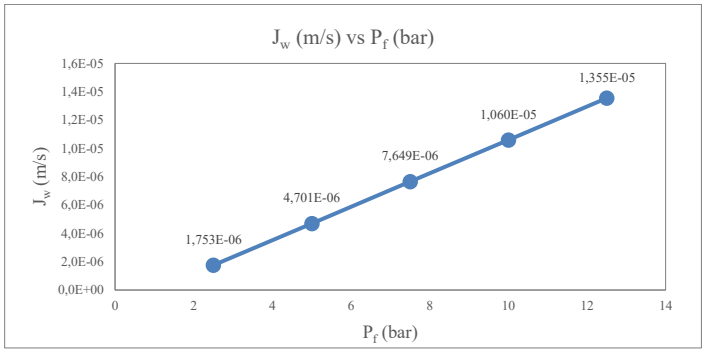

Fig 2. Solvent flux Jw (m/s) against P_f (bar) in hydraulic test

Beyond the local flux–pressure relation, it is important to check whether the axial variation of the bulk flow rates remains consistent with overall mass conservation. Figure 3 illustrates the axial profiles of the retentate flow rate $Q_f(z)$ and permeate flow rate $Q_p(z)$ along the dimensionless module length z/L for selected combinations of P_f and inlet flow rate $Q_{f,in}$. As water permeates through the membrane, $Q_f(z)$ decreases monotonically while $Q_p(z)$ increases, and both trends are close to linear under conditions where J_w is nearly uniform. This pattern confirms that the discretized model correctly couples the radial transport across the membrane with the longitudinal mass balance, similar to other axial-discretization approaches for nanofiltration modules used in process design and optimization [25].

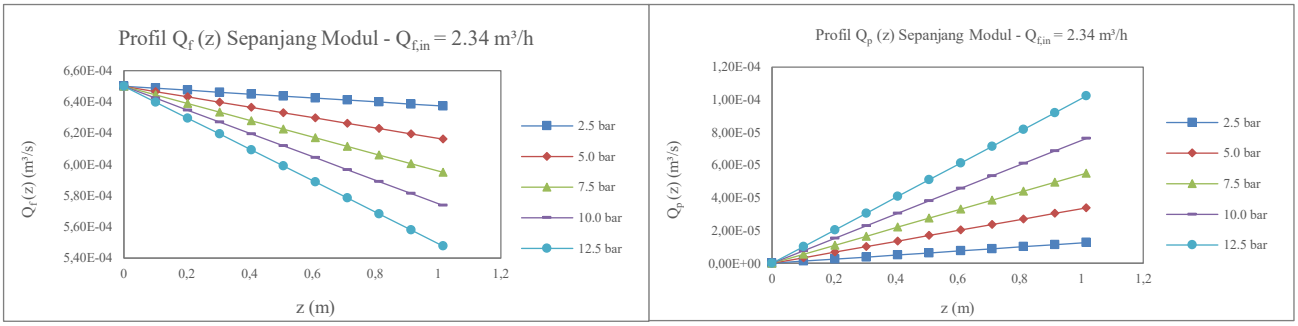

(a) (b)

Fig 3. Axial hydrodynamic behaviour of the NF module at $Q_{f,\text{in}} = 2.34\ \text{m}^3\text{h}^{-1}$ for different feed pressures P_f: (a) retentate flow rate $Q_f(z)$; (b) permeate flow rate $Q_p(z)$.

Taken together, **Fig 2**, **3(a)**, and **3(b)** provide a hydrodynamic "sanity check" for the model: the element behaves as expected for a spiral-wound NF module operated in cross-flow, with a nearly linear J_w - P_f relationship and smooth, monotonic evolution of Q_f and Q_p along the module, before moving on to more detailed analyses of recovery and ion-transport mechanisms in the following subsections.

3.2. Stage Recovery and Operating Window

Stage recovery is defined as the ratio between the permeate flow rate at the module outlet and the inlet feed flow rate, $\text{Rec} = Q_p(L)/Q_{f,in}$ (see Section 2.4). For a single-pass nanofiltration module operated at fixed hydraulic conditions, increasing the feed pressure P_f generally raises the solvent flux J_w, enlarges $Q_p(L)$, and therefore increases recovery. In contrast, increasing the inlet flow rate $Q_{f,in}$ mainly affects the denominator in the recovery expression, so that higher cross-flow tends to lower the stage recovery at constant pressure. This qualitative behavior is consistent with recent DSPM-DE based simulations and experiments on multi-ionic feeds, which report higher recoveries at larger transmembrane pressure but a systematic decrease in recovery as the feed flow or cross-flow velocity is increased [23].

Fig 4 summarizes the simulated end-of-module recovery as a function of $Q_{f,}$ for five feed-pressure levels (P_f =2.5 - 12.5 bar). A horizontal dashed line marks the design target of 15% recovery. At fixed pressure, the recovery curves decrease non-linearly as $Q_{f,in}$ is raised. The concave-down shape reflects the fact that, under the hydraulic scenario considered here, $Q_p(L)$ is controlled primarily by J_w and the available membrane area and is therefore only weakly dependent on $Q_{f,in}$, whereas the denominator in $\mathrm{Rec} = Q_p(L)/Q_{f,in}$ increases linearly with the feed flow. As a result, recovery approximately scales with $1/Q_{f,in}$ at constant P_f, reproducing the "recovery decreases with increasing feed flow" trend reported for NF treatment of multi-ionic solutions operated at different cross-flow velocities [23].

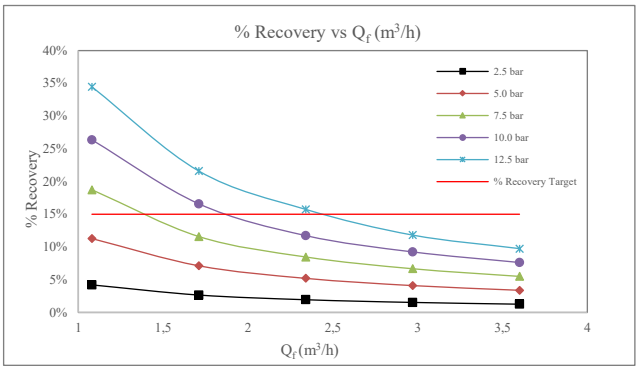

Fig 4. Simulated end-of-module recovery as a function of feed flow rate $Q_{f,in}$ for different feed pressures P_f; the dashed line indicates the design target of 15% recovery.

The second clear feature in Figure 4 is the upward shift of the entire recovery curve when P_f is increased. At the lowest feed flow ($Q_{f,in}$ =1.08 $m^3.h^{-1}$), the model predicts final recoveries of approximately 4, 11, 19, 26, and 34% for P_f = 2.5, 5.0, 7.5, 10.0, and 12.5 bar, respectively. This monotonic increase is expected because higher pressure directly raises the driving force for solvent transport and thus permeate production at fixed membrane area. Similar positive correlations between recovery and transmembrane pressure have been observed in long-term NF operation with ceramic and polymeric membranes, where recovery set-points between 40 - 80% are achieved by tuning the pressure window while monitoring fouling and salt rejection [26].

The 15% target line in Figure 4 provides a practical operating map for the KeenSen NF1-4040F element treating rejected brine. According to the simulations, value of $P_f = 12.5$ bar meets or exceeds the 15% recovery target up to approximately $Q_{f,in} \approx 2.4\ \mathrm{m^3 \cdot h^{-1}}$, whereas $P_f = 10$ bar satisfies the target up to $Q_{f,in} \approx 2.0\ \mathrm{m^3 \cdot h^{-1}}$. At $P_f = 7.5$ bar, the target is only reached for relatively low feed flow rates ($Q_{f,in} \lesssim 1.5\ \mathrm{m^3 \cdot h^{-1}}$), while 5.0 and 2.5 bar do not achieve 15% recovery within the investigated flow range. These trends align with NF design studies showing that higher pressure increases recovery but also strengthens concentration polarisation and the risk of scaling, whereas higher cross-flow mitigates polarisation at the cost of reduced single-pass recovery [27].

Overall, the simulated recovery map indicates that the design target of 15% can be attained by combining moderately high feed pressures with moderate feed flow rates, while lower-pressure operation would require either longer modules or multi-stage configurations to reach similar overall recovery. This compact representation of the operating window serves as a convenient first-screening tool before moving to more detailed analyses of ion transport, concentration profiles, and rejection performance in the following subsections [23][27].

3.3. Ion Rejection Performance: Divalent vs. Monovalent

Ion rejection is used as a compact metric for how effectively the nanofiltration membrane retains each species relative to its passage into the permeate stream. In this work, end-of-module rejection for ion i is defined on a molar-flow basis at the outlet segment, which is equivalent to the more common concentration–based form $100\ (1 - C_{i,P}/C_{i,F})$when the bulk volumetric flow is nearly constant. This definition is consistent with recent NF studies that treat rejection as a module-scale performance indicator directly linked to the mass balance of each ionic species [28]. Over the investigated operating window, the simulated end-of-module rejections fall into a clear hierarchy, with divalent ions strongly favored over monovalent ions (**Table 1**).

Table 1. Simulated end-of-module rejection ranges for each ion (baseline operating window)

Ion	Charge	%Rejection
Na^+	+1	74 – 75 %
Cl^-	-1	88 – 89 %
Ca^{2+}	+2	96.0 – 96.6 %
Mg^{2+}	+2	97.6 – 98.1 %
SO_4^{2-}	-2	99.0 – 99.3 %

The ordering $SO_4^{2-} > Mg^{2+} \gtrsim Ca^{2+} \gg Cl^- > Na^+$ reflects the combined action of steric hindrance, Donnan exclusion and dielectric exclusion in the DSPM-DE framework. Divalent ions experience a stronger electrostatic and dielectric penalty when entering the narrow pores, while monovalent ions are less strongly repelled and therefore display lower rejections.

This divalent ≫ monovalent pattern, together with improved rejection at higher cross-flow velocities, is consistent with recent ENP-based modelling and experimental work on charged NF membranes, which show that charge selectivity and dielectric exclusion dominate the separation of multi-ionic brines in the typical NF pore-size range [10][29][30].

For the monovalent cations and anions, Na^+ and Cl^-, the model predicts moderate rejections of ≈74 - 75% and ≈88 - 89%, respectively. Na^+ is the least rejected ion because it experiences the weakest combination of steric and electrostatic exclusion; its small hydrated radius and single positive charge make convective transport with the solvent flux the dominant mechanism, so that increases in transmembrane pressure tend to enhance Na^+ advection more than they enhance its electrostatic repulsion. Consequently, at fixed feed flow rate, raising feed pressure can slightly decrease the apparent Na^+ rejection in the low-to-moderate pressure region, a behavior also reported in NF studies of saline and surface waters when concentration-polarization is not fully controlled [31]. In contrast, increasing the cross-flow rate $Q_{f,in}$ systematically improves Na^+ and Cl^- rejection by thinning the concentration-polarization layer, lowering wall concentrations and moving the system closer to the intrinsic selectivity of the membrane; this trend aligns with hydrodynamic analyses that link higher cross-flow velocities to reduced CP and improved salt rejection [31][32].

The divalent cations Ca^{2+} and Mg^{2+} exhibit significantly higher rejections, in the ranges 96.0 - 96.6% and 97.6 - 98.1%, respectively. Their larger hydrated radii increase steric hindrance, while the double positive charge leads to stronger Donnan exclusion at the negatively charged membrane surface, so that only a small fraction of the incoming flux is transmitted to the permeate. As cross-flow increases, the benefit of reduced concentration-polarization is more modest than for monovalent ions because Ca^{2+} and Mg^{2+} are already strongly excluded by charge and dielectric effects; nevertheless, the simulations indicate a slight upward shift of rejection with $Q_{f,in}$, in line with experimental reports for brackish-water NF where divalent hardness ions remain > 95% rejected across a wide hydrodynamic window [10]. These results confirm that, within the investigated conditions, nanofiltration can consistently suppress Ca^{2+} and Mg^{2+} to levels suitable for high-purity salt production.

Sulfate (SO_4^{2-}) is the most strongly rejected species, with predicted rejections of 99.0 - 99.3% across the baseline operating window. This behavior is characteristic of multivalent anions in charged NF membranes, for which dielectric exclusion and Donnan partitioning act synergistically: the high valence and relatively large hydrated size of SO_4^{2-} create a substantial Born-energy penalty when moving from the high-dielectric bulk solution into the lower-dielectric pore environment, in addition to electrostatic repulsion by the negatively charged membrane matrix. Modern DSPM-DE studies emphasize that, for such anions, adjusting membrane charge density and pore dielectric constant is more effective for improving separation than simply increasing operating pressure, especially at intermediate–high salinity where Donnan exclusion alone is insufficient [30][33].

The very high SO_4^{2-} rejection predicted here is therefore consistent with the mechanistic understanding of NF and supports the feasibility of using the modelled module to strongly suppress sulfate impurities in rejected-brine feeds.

Overall, the rejection results summarized in Table 3 confirm that the KeenSen NF1-4040F module, operated within the investigated pressure and cross-flow window, behaves as a “hardness- and sulfate-selective” NF unit: divalent ions are almost completely retained, while monovalent ions are only partially rejected. This selectivity pattern matches the design objectives of producing higher-purity salt from rejected brine, where Ca^{2+}, Mg^{2+} and SO_4^{2-} are the primary impurities that must be minimized to avoid hygroscopicity and scaling issues in downstream industrial applications [10][29].

3.4. Axial Ion Fluxes and Concentration Profiles: Mechanistic Interpretation

To better understand the origin of the outlet rejection trends discussed in Section 3.3, this subsection examines the axial behaviour of ion fluxes and bulk concentrations along the NF module. Figure 5 shows the simulated axial profiles of the total ionic flux $J_i(z)$ for each species at a representative operating point (e.g. $P_f = 10$ bar and $Q_{f,in} = 2.34\ \mathrm{m^3 \cdot h^{-1}}$). These fluxes are obtained from the Extended Nernst-Planck (ENP) equation with Donnan, steric, and dielectric exclusion (DSPM-DE), as outlined in Section 2. The ENP formulation decomposes $J_i$conceptually into convective, diffusive, and electromigrative contributions; in practice, the model results confirm that convection dominates the net transport of most cations, while diffusion and electromigration play more prominent roles for anions, in agreement with recent mechanistic NF studies [17][23].

As shown in Figure 5, all ions exhibit positive fluxes that increase monotonically with axial position. The profiles are almost linear over most of the module length, reflecting the combination of (i) a decreasing retentate flow rate $Q_f(z)$, which leads to progressive concentration build-up, and (ii) a nearly uniform permeate-water flux $J_w$under the hydraulic conditions considered here. Because the convective term in the pores is proportional to $J_w$and to the local wall concentration $C_{i,w}(z)$, the convective contribution grows as the solution becomes more concentrated towards the module outlet. Diffusion opposes this convective transport by driving ions from the concentrated retentate side towards the permeate, whereas the electromigrative term adjusts to preserve local electroneutrality. Similar axial trends in $J_i(z)$ have been reported in other DSPM-DE simulations for multicomponent feeds, confirming that the present framework captures the essential coupling between hydrodynamics, ion transport, and charge balance in spiral-wound NF elements [23][25].

The relative magnitude of $J_i$across species follows the selectivity hierarchy expected for a negatively charged polyamide NF membrane. Monovalent ions (Na^+, Cl^-) present the highest fluxes, with J_{Na^+} typically larger than J_{Cl^-} because Na^+ experiences weaker electrostatic exclusion and is strongly dragged by the permeate flow. In contrast, the fluxes of divalent ions (Ca^{2+}, Mg^{2+}, SO_4^{2-}) are substantially lower and increase more slowly with z. This is a direct consequence of stronger steric hindrance, Donnan exclusion, and dielectric exclusion for multivalent species, particularly SO_4^{2-}, which faces the largest Born-energy penalty when entering the lower-dielectric pore environment. These mechanistic features are consistent with reported pore-scale partition coefficients and mobilities from detailed DSPM-DE analyses of tight NF membranes [10][17].

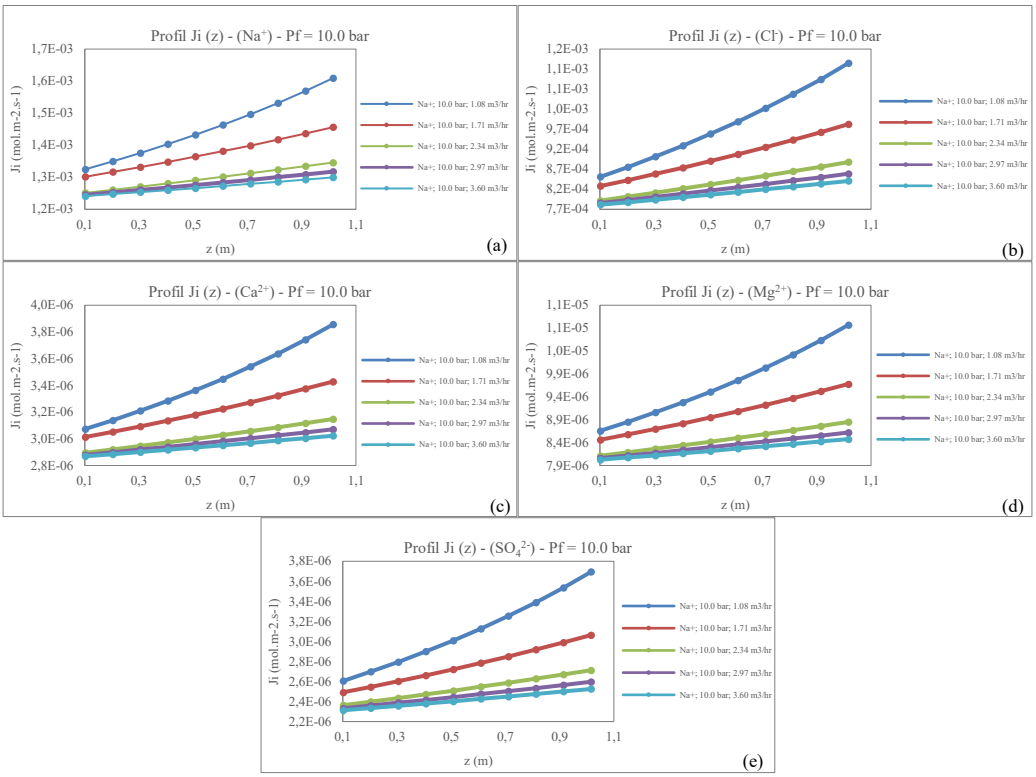

Fig 5. Simulated axial ionic flux profiles $J_i(z)$ at $P_f = 10.0$ bar for (a) Na^+, (b) Cl^-, (c) Ca^{2+}, (d) Mg^{2+}, and (e) SO_4^{2-} for different inlet feed flow rates $Q_{f_{in}}$ (1.08–3.60 $m^3 \cdot h^{-1}$).

Beyond the thorough-pore fluxes discussed above, the simulated axial bulk concentrations provide a complementary picture. Along the retentate channel, the model predicts that the retentate-side concentrations $C_{i,R}(z)$ of Na^+, Cl^-, Ca^{2+}, Mg^{2+}, and SO_4^{2-} increase monotonically with distance z as water is progressively removed, with steeper gradients at higher P_f and lower $Q_{f,in}$ where both recovery and concentration polarization are stronger. In physical terms, the combined effect of solvent permeation and limited back-diffusion leads to enrichment of all ionic species near the module outlet. Permeate-side concentrations $C_{i,P}(z)$ remain much lower than $C_{i,R}(z)$ for the strongly rejected ions, SO_4^{2-} and Mg^{2+} stay at very low levels along the entire module, whereas Na^+ and Cl^- exhibit higher and more rapidly increasing $C_{i,P}(z)$. This behaviour is consistent with classical concentration-polarization theory for NF/UF, which links retentate enrichment and mild flux decline to the build-up of solute in the boundary layer adjacent to the membrane surface [27].

Taken together, the axial flux and concentration profiles predicted by the model provide a mechanistic explanation for the outlet rejection hierarchy summarized in Section 3.3. The strong build-up of $C_{SO_4^{2-},R}(z)$ and $C_{Mg^{2+},R}(z)$, , combined with low permeate concentrations and relatively small fluxes for these ions, underpins the very high end-of-module rejections (≥97 - 99%) obtained for sulfate and magnesium. Conversely, the much larger convective fluxes and higher permeate concentrations of Na^+ and Cl^- naturally lead to lower overall rejections in the 70 - 90% range. Similar divalent ≫ monovalent selectivity and ion-specific axial trends have been reported in ENP/DSPM-DE studies of multi-ionic brines and seawater, reinforcing that the present modelling framework captures the relevant transport physics for nanofiltration of rejected brine in spiral-wound modules [17][23][25].

3.5. Mechanistic Transport Decomposition and Model Validation

To better interpret the overall rejection behavior, the total molar flux of each ionic species, J_i, was decomposed into the three contributions appearing in the Extended Nernst–Planck (ENP) equation, namely convection, diffusion, and electromigration. For a given operating condition, the local values of each mechanism were calculated across the membrane thickness and along the module length, then axially averaged to obtain representative percentages of $|J_{\mathrm{I,conv}}|$, $|J_{\mathrm{i,diff}}|$, and $|J_{\mathrm{i,elec}}|$ relative to $|J_i|$. This approach follows earlier ENP / DSPM-DE studies that use flux decomposition to link ion-specific selectivity to hydrodynamics and electrostatic exclusion [17][22][23] Table 3 summarizes the axial-average contribution of each mechanism for Na^+, Cl^-, Ca^{2+}, Mg^{2+}, and SO_4^{2-} over the investigated pressure window $P_f = 2.5 - 12.5$ bar at $Q_{f,in} = 2.34\ m^3 \cdot h^{-1}$. For Na^+, convection clearly dominates the transport, contributing approximately 75 - 80 % of the total flux, while electromigration contributes about 17 - 22 % and diffusion less than about 4 % across the entire pressure range. Cl^- displays a more balanced behavior, with convections contributing around 36 - 43 %, diffusion 34 - 37 %, and electromigration 23 - 28 %, reflecting its monovalent charge and weaker Donnan exclusion compared to the divalent ions.

For Ca^{2+}, the convective contribution is also very strong (≈ 78 - 82 %), whereas diffusion and electromigration account for roughly 15 - 17 % and 4 - 5 %, respectively, consistent with strong electrostatic and dielectric exclusion that limit back-diffusion of this divalent cation. Mg^{2+} shows the highest sensitivity to pressure: convection decreases from about 84 % at 2.5 bar to ≈71 % at 12.5 bar, while diffusion increases from ~10 % to ≈ 28 - 29 %, and electromigration remains relatively small (≈1.4 - 1.7 %). Finally, SO_4^{2-} exhibits a more even

split between convection and diffusion, with convective contributions decreasing from ~71 % to ~65 % and diffusion rising from ~23 - 24 % to ~26 - 27 % as pressure increases; electromigration for SO_4^{2-} lies in the range 6 - 8 %.

Table 2. Axial-average contribution of transport mechanisms to the total ionic flux for each species over $P_f = 2.5 - 12.5$ bar at $Q_{f,in} = 2.34\ m^3 \cdot h^{-1}$. percent ranges).

Ion	$J_{i,conv}$ (%)	$J_{i,diff}$ (%)	$J_{i,elec}$ (%)
Na^+	75 - 80	0 - 4	17 - 22
Cl^-	36 - 43	34 - 37	23 - 28
Ca^{2+}	78 - 82	15 - 17	4 - 5
Mg^{2+}	71 - 84	10 - 29	1 - 2
SO_4^{2-}	65 - 71	23 - 27	6 - 8

The patterns in **Table 2** provide a mechanistic interpretation of the rejection hierarchy discussed in Sections 3.3 and 3.4. For Na^+ and Ca^{2+}, the flux is primarily convective, with only modest diffusive counter-flux; these ions are carried forward with the permeating water, leading to comparatively lower rejections for Na^+ and intermediate rejections for Ca^{2+}. In contrast, SO_4^{2-} and Mg^{2+} experience strong Donnan and dielectric exclusion, which suppresses convective transport and enhances diffusive back-transport, thereby supporting very high overall rejections despite significant enrichment in the retentate. The nearly balanced contributions of convection, diffusion, and electromigration for Cl^- are consistent with its role as the main counter-ion that maintains electroneutrality within the pores, a behavior also reported in other multi-ionic DSPM-DE analyses of brines and seawater. From a modelling standpoint, this mechanistic decomposition is in good agreement with previous ENP / DSPM-DE applications, where convection typically dominates cation fluxes while anions, especially multivalent ones, show a larger share of diffusion and electromigration due to stronger electrostatic exclusion and the requirement of local electroneutrality [22][23][27].

Model validation was carried out at two levels. First, internal numerical checks were performed to ensure the consistency of the coupled radial–axial solution. For all simulated conditions, the global mass balance for water and each ionic species closed within a small numerical tolerance, and the electroneutrality condition was satisfied in both retentate and permeate streams. The nearly linear relation between solvent flux J_w and transmembrane pressure in the hydraulic test (Section 3.1) further supports that the hydraulic permeability and osmotic-pressure corrections are correctly implemented in the model. Second, the model predictions were compared against experimental data from the literature for nanofiltration of brines and multi-ionic electrolyte solutions using commercial polyamide NF membranes. In particular, the simulated trends in water flux and divalent-ion rejection are consistent with the high Mg^{2+} and SO_4^{2-} rejections (≥95 - 99 %) reported for NF90 and other tight NF membranes, while the lower Na^+ and Cl^- rejections predicted here agree with the typical divalent » monovalent selectivity observed in experimental studies of seawater and SWRO brines [10][16][27] Overall, the combination of mechanistic flux decomposition, internal numerical consistency, and agreement with independent literature data indicates that the present DSPM-DE model provides a physically sound and semi-quantitatively reliable description of ion transport in the KeenSen NF1-4040F element treating rejected brine.

4. Conclusion

This study developed and applied a coupled DSPM-DE/Extended Nernst–Planck model for a spiral-wound KeenSen NF1-4040F element treating multi-ionic rejected brine, with the aim of predicting water flux, recovery, and ion-specific rejection as a function of feed pressure and inlet flow rate. The hydraulic verification showed a nearly linear $J_w - P_f$ relationship and consistent axial mass balances, confirming that the implemented permeability and pressure–drop relations are physically sound. The recovery maps revealed that a target single-pass recovery of around 15% can be achieved by combining moderate-to-high feed pressures with intermediate feed flow rates, while the axial profiles of concentrations and ionic fluxes clarified how retentate enrichment and through-pore transport evolve along the module. Mechanistic flux decomposition demonstrated that cation transport, especially Na^+ and Ca^{2+}, is strongly convection-dominated, whereas diffusion and electromigration contribute a larger fraction to anion transport, particularly for SO_4^{2-} and, to a lesser extent, Cl^-. As a result, the model reproduces a clear divalent ≫ monovalent selectivity, with very high rejections for SO_4^{2-}, Mg^{2+}, and Ca^{2+} and lower, but still significant, rejections for Na^+ and Cl^-, providing a coherent process-scale explanation for the observed separation hierarchy.

From an application perspective, these results support the use of nanofiltration as a selective pre-purification step to upgrade rejected brine into a higher-purity feed for industrial salt production, by strongly suppressing hardness and sulfate while allowing part of the NaCl to pass. At the same time, the study highlights key modelling limitations, such as the simplified treatment of osmotic effects and concentration polarisation, the assumption of ideal solution properties, and the neglect of fouling and ageing, that point to natural extensions of this work. Future research should incorporate more detailed CP correlations and osmotic-pressure corrections, calibrate membrane parameters via dedicated experiments and inverse modelling, and couple the transport model with energy and cost analyses to optimise $P_f - Q_{f,}$ - recovery trade-offs. In the longer term, extending the framework to multi-stage or recycle configurations and embedding fouling/aging dynamics would further enhance its value as a design and optimisation tool for valorising rejected brine in industrial salt supply chains.

Acknowledgement

The authors gratefully acknowledge the Department of Chemical Engineering, Institut Teknologi Sepuluh Nopember (ITS), for providing the computational facilities and academic environment that supported this work. The first author would like to thank Dr. Ir. Susianto, DEA

and Prof. Dr. Ir. Ali Altway, M.Sc. for their continuous guidance, constructive discussions, and supervision during the development of the mathematical model and the preparation of this manuscript.
This research was carried out as part of the Master's thesis of the first author at ITS. The authors also appreciate the technical and administrative assistance provided by colleagues in the graduate programme and laboratory staff.

References

[1] I. H. Saputra, T. Mariyanti, and M. R. Athallah, "Strategy For Development of Pharmaceutical Salt Business in Improving The Welfare of The Salt Farmers from Islamic Perspective," *ADI Journal on Recent Innovation (AJRI)*, vol. 4, no. 1, pp. 43–55, Jun. 2022, doi: 10.34306/ajri.v4i1.750.
[2] E. Jones, M. Qadir, M. T. H. van Vliet, V. Smakhtin, and S. mu Kang, "The state of desalination and brine production: A global outlook," Mar. 20, 2019, *Elsevier B.V.* doi: 10.1016/j.scitotenv.2018.12.076.
[3] M. Omerspahic, H. Al-Jabri, S. A. Siddiqui, and I. Saadaoui, "Characteristics of Desalination Brine and Its Impacts on Marine Chemistry and Health, With Emphasis on the Persian/Arabian Gulf: A Review," Apr. 26, 2022, *Frontiers Media S.A.* doi: 10.3389/fmars.2022.845113.
[4] Y. EL Idrissi, M. Benabbou, Z. Rais, and M. EL Haji, "Brackish and seawater pretreatment processes: A systematic literature review," *Desalination Water Treat*, vol. 318, Apr. 2024, doi: 10.1016/j.dwt.2024.100350.
[5] A. A. Izadpanah and A. Javidnia, "The ability of a nanofiltration membrane to remove hardness and ions from diluted seawater," *Water (Switzerland)*, vol. 4, no. 2, pp. 283–294, 2012, doi: 10.3390/w4020283.
[6] M. E. A. Ali, "Nanofiltration Process for Enhanced Treatment of RO Brine Discharge," *Membranes (Basel)*, vol. 11, no. 3, pp. 1–6, Mar. 2021, doi: 10.3390/membranes11030212.
[7] M. Avramidi *et al.*, "Optimization of the Quality of Reclaimed Water from Urban Wastewater Treatment in Arid Region: A Zero Liquid Discharge Pilot Study Using Membrane and Thermal Technologies," *Membranes (Basel)*, vol. 15, no. 7, Jul. 2025, doi: 10.3390/membranes15070199.
[8] O. Agboola, J. Maree, A. Kolesnikov, R. Mbaya, and R. Sadiku, "Theoretical Performance of Nanofiltration Membranes for Wastewater Treatment," Mar. 01, 2015, *Springer Verlag, Pretoria*. doi: 10.1007/s10311-014-0486-y.
[9] Y. Roy, D. M. Warsinger, and J. H. Lienhard, "Effect of temperature on ion transport in nanofiltration membranes: Diffusion, convection and electromigration," *Desalination*, vol. 420, pp. 241–257, 2017, doi: 10.1016/j.desal.2017.07.020.
[10] A. Saavedra, H. Valdés, J. Velásquez, and S. Hernández, "Comparative Analysis of Donnan Steric Partitioning Pore Model and Dielectric Exclusion Applied to The Fractionation of Aqueous Saline Solutions through Nanofiltration," *ChemEngineering*, vol. 8, no. 2, Apr. 2024, doi: 10.3390/chemengineering8020039.
[11] N. Cevallos-Cueva, M. M. Rahman, H. H. Kinfu, and V. Abetz, "Mass Transport Mechanisms Insights of Selective Sodium / Magnesium Separation Through Nanofiltration Membranes," *J Memb Sci*, vol. 721, Apr. 2025, doi: 10.1016/j.memsci.2025.123808.
[12] Y. Roy, M. H. Sharqawy, and J. H. Lienhard V., "Modeling of Flat-Sheet and Spiral-Wound Nanofiltration Configurations and its Application in Seawater Nanofiltration," *J Memb Sci*, vol. 493, pp. 360–372, Nov. 2015, doi: 10.1016/j.memsci.2015.06.030.
[13] W. R. Bowen and J. S. Welfoot, "Modelling the performance of membrane nanoÿltration-critical assessment and model development," 2002. [Online]. Available: www.elsevier.com/locate/ces
[14] O. Labban, C. Liu, T. H. Chong, and J. H. Lienhard V., "Fundamentals of Low-Pressure Nanofiltration: Membrane Characterization, Modeling, and Understanding The Multi-Ionic Interactions in Water Softening," *J Memb Sci*, vol. 521, pp. 18–32, Jan. 2017, doi: 10.1016/j.memsci.2016.08.062.
[15] N. S. Suhalim *et al.*, "Rejection Mechanism of Ionic Solute Removal by Nanofiltration Membranes: An Overview," Feb. 01, 2022, *MDPI*. doi: 10.3390/nano12030437.
[16] M. Figueira, D. Rodríguez-Jiménez, J. López, M. Reig, J. Luis Cortina, and C. Valderrama, "Evaluation of the nanofiltration of brines from seawater desalination plants as pre-treatment in a multimineral brine extraction process," *Sep Purif Technol*, vol. 322, Oct. 2023, doi: 10.1016/j.seppur.2023.124232.
[17] N. Cevallos-Cueva, M. M. Rahman, H. Hailu Kinfu, and V. Abetz, "Mass Transport Mechanism of Nitrate Selective Nanofiltration Membranes on The Basis of The Donnan Steric Pore Model With Dielectric Exclusion (DSPM-DE)," *Chemical Engineering Journal*, vol. 493, Aug. 2024, doi: 10.1016/j.cej.2024.152775.
[18] Z. Ma, M. Wang, X. Gao, and C. Gao, "Charge and separation characteristics of nanofiltration membrane embracing dissociated functional groups," *Front Environ Sci Eng*, vol. 8, no. 5, pp. 650–658, 2014, doi: 10.1007/s11783-013-0605-1.
[19] W. R. Bowen and J. S. Welfoot, "Modelling the performance of membrane nanoÿltration-critical assessment and model development," 2002. [Online]. Available: www.elsevier.com/locate/ces
[20] M. Micari *et al.*, "Experimental and Theoretical Characterization of Commercial Nanofiltration Membranes for the Treatment of Ion Exchange Spent Brine."
[21] S. Bandini and D. Vezzani, "Nanofiltration Modeling: The Role of Dielectric Exclusion in Membrane Characterization," *Chem Eng Sci*, vol. 58, no. 15, pp. 3303–3326, 2003, doi: 10.1016/S0009-2509(03)00212-4.
[22] A. Szymczyk, Y. Lanteri, and P. Fievet, "Modelling the transport of asymmetric electrolytes through nanofiltration membranes," *Desalination*, vol. 245, no. 1–3, pp. 396–407, Sep. 2009, doi: 10.1016/j.desal.2009.02.003.
[23] A. Ghorbani, B. Bayati, E. Drioli, F. Macedonio, T. Kikhavani, and M. Frappa, "Modeling of nanofiltration process using dspm-de model for purification of amine solution," *Membranes (Basel)*, vol. 11, no. 4, Apr. 2021, doi: 10.3390/membranes11040230.
[24] S. Shahgodari, J. Labanda, and J. Llorens, "Experimental and Modeling Study of the Nanofiltration of Alcohol-Based Molecules and Amino Acids by Commercial Membranes," *Membranes (Basel)*, vol. 13, no. 7, Jul. 2023, doi: 10.3390/membranes13070631.
[25] T. Hubach, S. Schlüter, and C. Held, "Model-Based Optimization of Multi-Stage Nanofiltration Using the Solution-Diffusion–Electromigration Model," *Processes*, vol. 11, no. 8, Aug. 2023, doi: 10.3390/pr11082355.
[26] S. M. Cabrera, L. Winnubst, H. Richter, I. Voigt, J. McCutcheon, and A. Nijmeijer, "Performance evaluation of an industrial ceramic nanofiltration unit for wastewater treatment in oil production," *Water Res*, vol. 220, Jul. 2022, doi: 10.1016/j.watres.2022.118593.

[27] A. Giacobbo, A. M. Bernardes, M. J. F. Rosa, and M. N. De Pinho, "Concentration polarization in ultrafiltration/nanofiltration for the recovery of polyphenols from winery wastewaters," *Membranes (Basel)*, vol. 8, no. 3, Sep. 2018, doi: 10.3390/membranes8030046.

[28] B. Thabo, B. J. Okoli, S. J. Modise, and S. Nelana, "Rejection capacity of nanofiltration membranes for nickel, copper, silver and palladium at various oxidation states," *Membranes (Basel)*, vol. 11, no. 9, Sep. 2021, doi: 10.3390/membranes11090653.

[29] A. Popova, R. Rattanakom, Z. Q. Yu, Z. Li, K. Nakagawa, and T. Fujioka, "Evaluating the potential of nanofiltration membranes for removing ammonium, nitrate, and nitrite in drinking water sources," *Water Res*, vol. 244, Oct. 2023, doi: 10.1016/j.watres.2023.120484.

[30] D. Lu, Z. Yao, L. Jiao, M. Waheed, Z. Sun, and L. Zhang, "Separation mechanism, selectivity enhancement strategies and advanced materials for mono-/multivalent ion-selective nanofiltration membrane," Jan. 01, 2022, *KeAi Communications Co.* doi: 10.1016/j.advmem.2022.100032.

[31] K. Tonova *et al.*, "Separation of glucose, other reducing sugars and phenolics from natural extract by nanofiltration: Effect of pressure and cross-flow velocity," *Chemical Engineering Research and Design*, vol. 162, pp. 107–116, Oct. 2020, doi: 10.1016/j.cherd.2020.07.030.

[32] D. Q. Lai, N. Tagashira, S. Hagiwara, M. Nakajima, T. Kimura, and H. Nabetani, "Influences of technological parameters on cross-flow nanofiltration of cranberry juice," *Membranes (Basel)*, vol. 11, no. 5, May 2021, doi: 10.3390/membranes11050329.

[33] G. Bargeman, O. Guerra Miguez, J. B. Westerink, and A. ten Kate, "Chloride retention model for concentrated solutions containing sodium chloride and sodium sulfate based on thermodynamic considerations," *Desalination*, vol. 555, Jun. 2023, doi: 10.1016/j.desal.2023.116562.